Imaging Local Heating and Thermal Diffusion of Nanomaterials with Plasmonic Thermal Microscopy

Zixuan Chen,[†] Xiaonan Shan,[*,‡] Yan Guan,[‡] Shaopeng Wang,[‡] Jun-Jie Zhu,[*,†] and Nongjian Tao[*,†]

[†]State Key Laboratory of Analytical Chemistry for Life Science and Collaborative Innovation Center of Chemistry for Life Sciences, School of Chemistry and Chemical Engineering, Nanjing University, Nanjing 210093, China and [‡]Center for Bioelectronics and Biosensors, Biodesign Institute, Arizona State University, Tempe, Arizona 85287, United States

ABSTRACT Measuring local heat generation and dissipation in nanomaterials is critical for understanding the basic properties and developing applications of nanomaterials, including photothermal therapy and joule heating of nanoelectronics. Several technologies have been developed to probe local temperature distributions in nanomaterials, but a sensitive thermal imaging technology with high temporal and spatial resolution is still lacking. Here, we describe plasmonic thermal microscopy (PTM) to image local heat generation and diffusion from nanostructures in biologically relevant aqueous solutions. We demonstrate that PTM can detect local temperature change as small as 6 mK with temporal resolution of 10 μs and spatial resolution of submicrons (diffraction limit). With PTM, we have successfully imaged photothermal generation from single nanoparticles and graphene pieces, studied spatiotemporal distribution of temperature surrounding a heated nanoparticle, and observed heating at defect sites in graphene. We further show that the PTM images are in quantitative agreement with theoretical simulations based on heat transport theories.

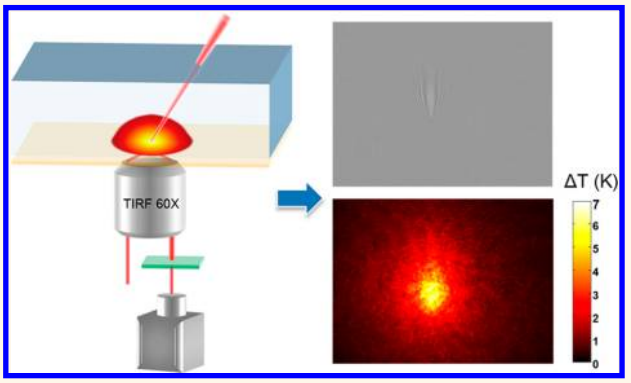

KEYWORDS: plasmonic · thermal microscopy · thermal diffusion · gold nanorods · photothermal

The ability to image local temperature changes with high spatial and temporal resolutions is critical for us to understand the basic thermal properties of micro- and nanostructured materials, including biological systems. This capability is also important for us to develop applications with nanomaterials, such as photothermal therapy with nanoparticles, local chemical reactions of catalytic nanoparticles, and heat dissipation in nanoelectronic circuits.[1−4] Substantial advances have been made in recent years to develop such a capability, and the technologies reported to date fall into two categories: scanning probe and nonscanning probe based strategies. The former includes scanning thermal microscopy (SThM),[5−8] scanning photothermal microscopy,[9−14] plasmon energy expansion thermometry,[15] and Raman thermometry,[1,16] and the latter includes methods using nanodiamonds,[17,18] nanothermometers,[19] fluorescent probes,[20−23] thermal microscopy,[24] and infrared cameras.[25] Each technology has its own unique strengths but also distinct weaknesses. For example, SThM provides high spatial resolution (down to ~10 nm) and high sensitivity (on the order of mK),[5−8] but the scanning of a probe slows down the imaging speed and makes it difficult to detect local temperature inside a biological cell. For biological applications and chemical analysis, it is also important to be able to image heat generation and dissipation in aqueous solutions and to map the fast spatiotemporal distributions of heat dissipation *via* thermal diffusion in the solutions.

We report here plasmonic thermal microscopy (PTM) to image heat generation and dissipation from nanomaterials in aqueous solutions with high temperature sensitivity and temporal resolution. We have demonstrated the working principle of PTM, examined its sensitivity, and compared the measured thermal images with theoretical

* Address correspondence to xiaonan.shan@asu.edu, jjzhu@nju.edu, njtaob@gmail.com.

Received for review August 24, 2015 and accepted October 4, 2015.

Published online 10.1021/acsnano.5b05306

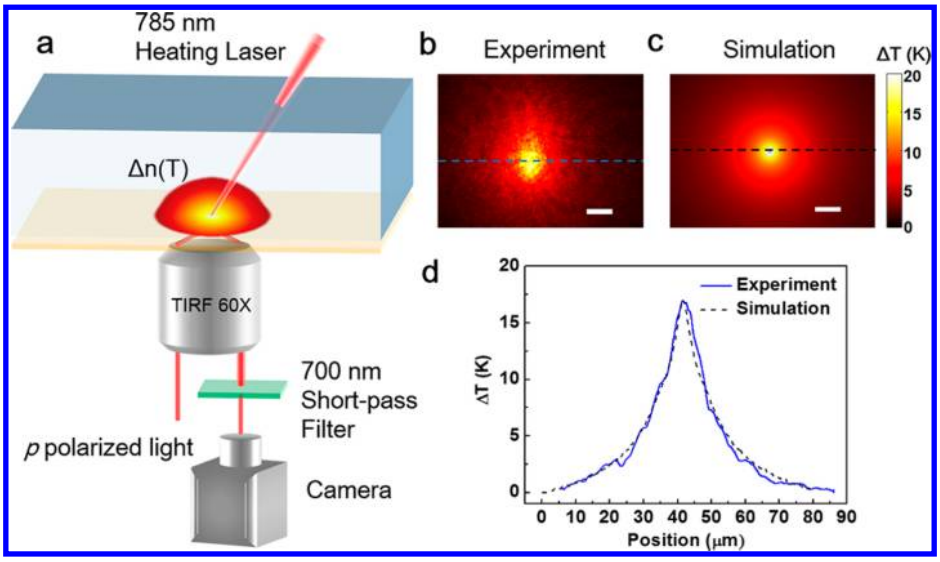

Figure 1. Experimental setup and principle demonstration of PTM. (a) Schematic illustration PTM setup and principle. A 785 nm heating laser is focused on a gold-coated glass slide to generate a localized heat, which leads to a refractive index change of the surrounding medium (water). This refractive index change is imaged by plasmonic imaging using an inverted optical microscope with a high numerical aperture objective. The plasmonic imaging uses p-polarized light to excite surface plasmons on the gold surface and CCD imager to record the reflected beam. To remove interference from the heating laser, a short-pass optical filter is placed before the CCD imager. (b) Measured PTM image of temperature distribution generated by a focused laser with power of 240 mW/μm^2. (c) Finite element analysis simulation of temperature distribution. Scale bar: 10 μm. (d) Spatial profile of the thermal distribution along the dashed line shown in (b) and (c) showing good agreement between the experimental and simulated temperature distributions.

simulations. We have further shown that PTM can be operated in two modes, scanning a focused laser beam across a sample line by line or illuminating the entire sample with light to map the local temperature of the illuminated area simultaneously. Using PTM, we have measured local temperature and its spatiotemporal distribution associated with the heating of single nanoparticles and studied the photothermal properties of graphene.

RESULTS AND DISCUSSION

Imaging Principle and Calibration. PTM is based on the temperature dependence of the refractive index, which is detected with surface plasmon resonance (SPR) with high sensitivity. The working principle and experimental setup of PTM are illustrated in Figure 1a. The setup is based on an inverted optical microscope with a high numerical aperture oil immersion objective. Placed on the objective is a gold-coated glass slide, on which a polydimethylsiloxane (PDMS) cell is attached to hold solution. p-Polarized light with a wavelength of 680 nm from a superluminescent diode (SLD) is directed onto a gold-coated cover glass (47 nm gold film) with an appropriate incident angle *via* the objective to excite surface plasmons on the gold surface. The reflected light is collected with the same objective to form a SPR image, which is recorded with a fast CCD camera. To demonstrate thermal imaging with PTM, local heating is generated by focusing a laser beam from the top onto the gold film. The wavelength of the heating laser is 785 nm,[26] and the focused spot has a diameter of about 1 μm. The heating laser generates a local temperature increase, which causes a decrease in the refractive index (n) of the medium (water) near the gold surface.[10] The spatial distribution of the refractive index change ($\Delta n(x,y)$) is imaged by PTM, from which the local temperature is determined based on the following formalism.[27−30]

The refractive index change (Δn) is directly related to temperature change (ΔT), which can be obtained from the local SPR signal change according to

$$\Delta T = \frac{\partial T}{\partial \theta}\Delta\theta = \frac{1}{\frac{\partial n}{\partial T}}\cdot\frac{1}{\frac{\partial \theta}{\partial n}}\cdot\Delta\theta \qquad (1)$$

where θ is the SPR resonant angle, $\partial n/\partial T$ is the temperature coefficient of the refractive index, and $\partial\theta/\partial n$ is the SPR sensitivity. For water, $\partial n/\partial T$ and $\partial\theta/\partial n$ are -10^{-4} K^{-1} and 136.4 deg/RIU near room temperature, respectively, where RIU is relative refractive index unit, or $\Delta n/n$ (Figure S2). If we denote that $\alpha = \partial n/\partial T$ and $\beta = \partial\theta/\partial n$, then eq 1 is simplified as

$$\Delta T(x,y,t) = \frac{1}{\alpha\cdot\beta}\cdot\Delta\theta(x,y,t) \qquad (2)$$

Using the water α and β values given above, we have $1/\alpha\cdot\beta = -73.3$ K deg^{-1}, which allows us to determine local temperature from the measured SPR image.

To demonstrate the principle of PTM, we imaged local thermal distribution generated by the heating laser with an intensity (I_{exp}) of 240 mW/μm^2 (Figure 1b). The heating laser was focused to a spot on the gold surface, producing a temperature distribution around the heating spot. The PTM image of the temperature

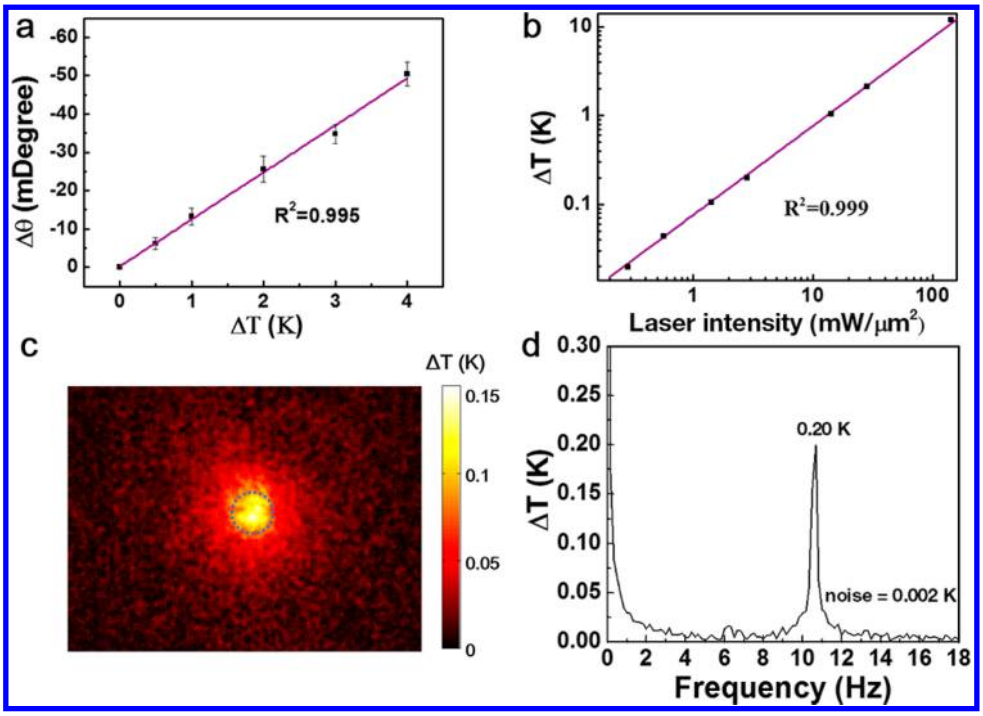

Figure 2. Detection limit and sensitivity of PTM. (a) Calibration curve illustrating the linear relationship between temperature and SPR resonant angle shift. (b) Linear relationship between heating laser intensity and the detected temperature increase. (c) PTM image of temperature distribution generated by 2.8 mW/μm^2 heating laser. (d) Fourier spectrum of temperature measured with PTM within the region marked with a dashed circle in (c).

distribution ($\Delta T(x,y)$) is shown in Figure 1b using eq 2. The temperature at the center of the heating spot is ~20 K above the background temperature, which decreases rapidly from the center, as shown in Figure 1d. Using a COMSOL model to solve the heat transport equation with appropriate initial and boundary conditions, we obtained simulated temperature distribution (details are described in the Methods). The simulated temperature distribution (Figure 1c,d) is in excellent agreement with the experimental data. Note that the COMSOL simulation assumes an optical absorption efficiency of ~3.4%, which is consistent with the calculation by the transfer matrix method, a method widely used to calculate optical properties of thin layers.[26,31]

Equation 2 predicts that the temperature change (ΔT) is proportional to the resonant angle shift ($\Delta\theta$). To calibrate the relationship between ΔT and $\Delta\theta$, we performed the following calibration experiment. A microthermistor was immersed in the solution and placed on the gold surface to monitor the temperature in real time. The thermistor output signal was synchronized with PTM imaging with a data acquisition (DAQ) card. The solution was heated by adding hot deionized water, followed by stirring the solution with a pipet to ensure a uniform temperature of the solution. The measured $\Delta\theta$ and ΔT are plotted in Figure 2a, showing a linear relationship. By fitting the data with eq 2, $1/\alpha\cdot\beta$ was found to be -75.8 K deg^{-1}, which is consistent with the value determined from the thermal coefficient of water and SPR sensitivity as discussed earlier. Note that the resonant angle shift ($\Delta\theta$) was obtained from SPR image intensity, which was calibrated with ethanol at different concentrations (different refractive indices). The measurement was performed at a fixed incident angle, where the SPR image intensity changes linearly with the shift in the resonant angle.[32−34] We also determined temperature change, ΔT, *versus* the heating laser intensity varying from 0 to 141 mW/μm^2 (Figure S3), which shows a linear relationship (Figure 2b).

Sensitivity Analysis. To achieve a good detection limit, we created a small periodic oscillation in temperature by modulating the heating laser power with an amplitude of 2.8 mW/μm^2 and a frequency of 10.6 Hz. Because of the large thermal diffusivity of the system, the temperature response is 0.1 ms, which is sufficiently fast to respond to the 10.6 Hz temperature modulation (Figure 4c and Figure S4). We obtained the temperature modulation in every pixel by performing fast Fourier transform (FFT) analysis on the plasmonic image.[35,36] The FFT spectrum of each pixel revealed a peak located at 10.6 Hz. By converting the peak amplitude into temperature with the calibration curve shown in Figure 2a, we obtained a PTM image with an image intensity representing the local temperature (Figure 2c) (details are in the Methods section). The FFT spectrum of the center of the heating spot is plotted in Figure 2d, showing a peak at 10.6 Hz. The peak amplitude corresponds to a temperature increase of 0.2 K with a noise level of ~2 mK. If we use 3 times

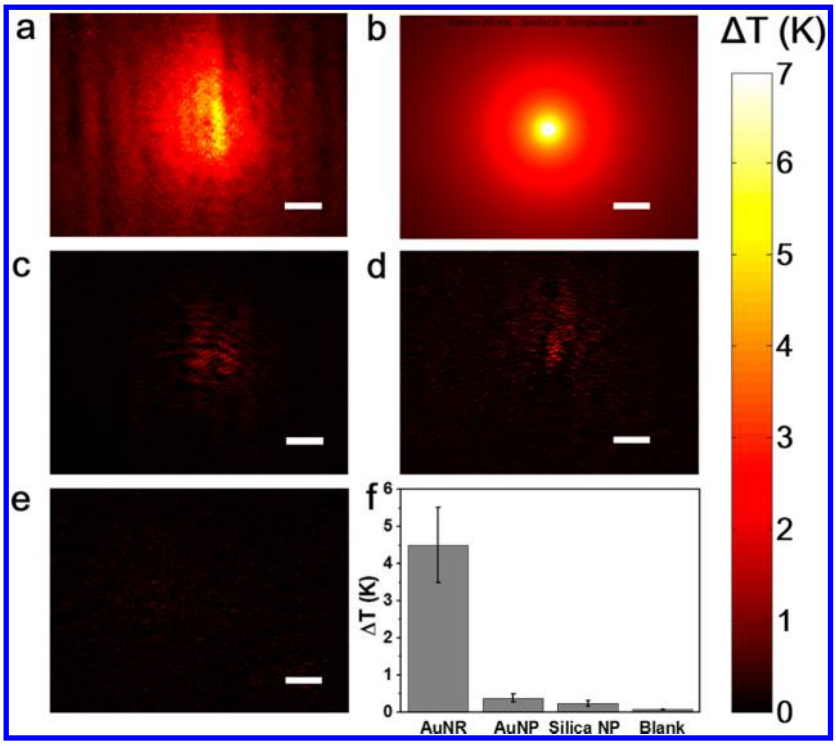

Figure 3. Heat generation and temperature distribution of single GNR. (a) Measured PTM image of temperature distribution generated by a single heated gold nanorod. (b) Corresponding simulated temperature distribution generated by the gold nanorod. (c–e) Measured PTM images of a single gold nanoparticle (c), single silica nanoparticle (d), and blank area (e) illuminated with a 240 mW/μm^2 heating laser. Scale bar: 10 μm. (f) Average temperature increases for the gold nanorods, gold nanoparticles, silica nanoparticles, and blank area of gold surface.

the noise level as the detection limit, then the detection limit of PTM is estimated to be 6 mK. The noise of the system is determined by mechanical drift, light source stability, and ambient temperature variations. By modulating heating at a frequency (~10–20 Hz) and detecting the response, we find that the noise at frequencies other than the modulation frequency is rejected.

Thermal Image of Single Gold Nanorod. To further evaluate PTM capability for imaging temperature distribution in nanomaterials, we imaged the temperature distribution generated by heating gold nanorods (GNRs). The plasmonic image of a GNR has a parabolic pattern (Figure S5), which originates from the scattering of the plasmonic wave by the GNR.[27] The GNRs have an optical absorption peak at 750 nm (Figure S6), which is close to the wavelength of the heating laser, thus providing efficient heating. The heating laser was modulated at 10.6 Hz to create PTM images of the heated GNRs according to the procedure described above. To obtain a clear PTM image of the GNRs, we subtracted background heat generation in the area without GNRs.

Figure 3a shows the temperature distribution generated by heating a single GNR with a diameter and length of 40 and 150 nm, respectively. The temperature increase can reach 6 K by the heating laser with an intensity of 240 mW/μm^2. The corresponding simulated temperature distribution image is shown in Figure 3b, which matches well with that of the experimental PTM image. Note that the temperature distribution measured by PTM (Figure 3a) shows slight elongation compared to the simulation result (Figure 3b). This is caused by the propagation of surface plasmon wave along the elongation direction. The effective heating intensity used in the simulation was 30 mW/μm^2, from which the optical absorption efficiency of a single GNR was estimated to be 12.5%, ~4 times higher than that of the gold film. The higher efficiency is expected because the wavelength of the heating laser was close to the absorption peak of GNRs.[37] To confirm this observation, control experiments were carried out using 60 nm diameter gold nanoparticles (GNPs), 540 nm silica nanoparticles (silica NPs), and a blank sample (without any particle), which show little contrast in the PTM images (Figure 3c–e). The UV–vis spectra (Figure S6) show weak optical absorption of the gold and silica nanoparticles at the heating laser wavelength of 785 nm. Statistical analysis over 30 samples showed that the average temperature increase of GNRs was more than 4 K, while the average temperature increases for GNPs and silica NPs were only 0.4 and 0.21 K, respectively, and the background (blank) temperature variation was 0.07 K (Figure 3f). These results support the interpretation of the PTM images.

Imaging Heat Diffusion from a Single Nanoscale Object. The results described above have demonstrated the PTM

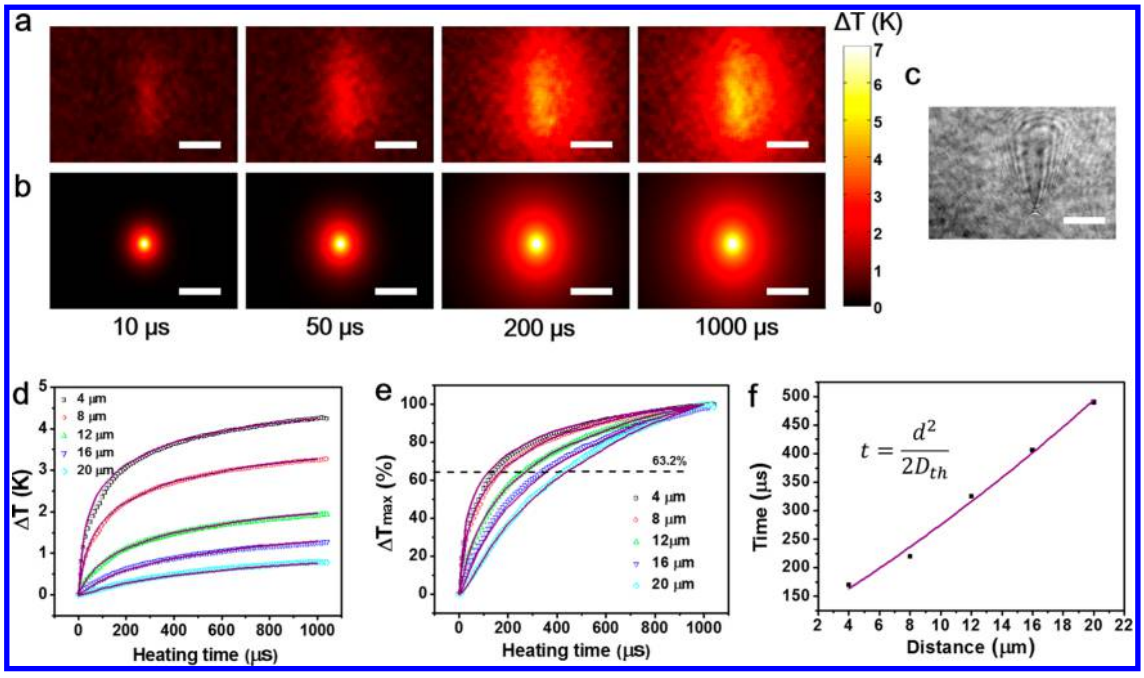

Figure 4. Imaging of heat diffusion dynamics from a single GNR. (a,b) Snapshots of measured (a) and simulated (b) thermal images of transient thermal diffusion processes that resulted from heating a gold nanorod with laser with intensity of 240 mW/μm^2. Scale bar: 10 μm. (c) Plasmonic image of the gold nanorod in (a), showing a parabolic tail. Scale bar: 10 μm. (d) Measured (symbols) and simulated (lines) local temperatures at various distances from the gold nanorod. (e) Normalized presentation of the data in (c). (f) Characteristic time constant required to reach 63.2% of maximum temperature change (from (e)) at different distances from the gold nanorod.

capability for imaging steady-state temperature distribution surrounding a heated nanoscaled material. Imaging transient thermal diffusion processes from the nanomaterials requires high temporal resolution, which has been a difficult task with previous technologies.[6,38] We show below that PTM can map the time evolution of the temperature distribution of nanomaterials. The transient change in the temperature distribution is determined by thermal diffusion, which is on the order of microseconds over a range of a few microns in water (see Supporting Information for details). To reach this fast imaging speed with PTM, a high-speed camera (frame rate up to 120000 fps) was used to capture the fast transient heat diffusion process due to the heating of single GNRs.

The measurement was carried out by aiming the heating laser at a single GNR and suddenly turning on the laser at time 0. In contrast, to periodically modulate the heating laser (Figures 2 and 3), we switched on the heating laser to heat the GNR at $t = 0$. Consequently, the GNR was heated, and the generated heat was diffused away from the GNR. This transient heat transport process was recorded by PTM and is presented as a movie (movie S1). Figure 4a displays several snapshots at different stages of the fast transient heat transport process. Note that the rise time of the heating laser is much faster than 10 μs (Figure S7), so that the transient change in the temperature distribution measured by PTM was purely due to heat transport. In order to verify the thermal diffusion process observed with PTM, numerical simulation was carried out, and the simulation results as shown in Figure 4b and movie S2 agree well with the experimental data.

Figure 4d plots both measured and simulated transient temperature profiles at 4, 8, 12, 16, and 20 μm away from the GNR. The simulated temperature profiles fit the experimental profiles well, both showing a rapid initial rise in temperature followed by a slow increase. The maximum temperatures at $t = 1000$ μs at 4 and 20 μm away from the GNR were 4.2 and 0.8 K, respectively. To illustrate more clearly different diffusion time constants at different locations and extract thermal diffusivity, we normalized the temperature profiles by the temperatures at $t = 1000$ μs, which is shown in Figure 4e. From the temperature profiles, the time constant for heat to diffuse and reach 63.2% of maximum temperature was extracted, which is plotted *versus* distance to the GNR. The thermal diffusion time (t) and distance (d) are related by $t = d^2/2D_{th}$, where D_{th} is thermal diffusivity. By fitting the temperature profiles with this equation, we have extracted thermal diffusivity, $D_{th} = 2.55 \times 10^{-7}$ m^2/s; this value agrees with the simulation result (2.38×10^{-7} m^2/s). The number between water (1.43×10^{-7} m^2/s) and glass (3.4×10^{-7} m^2/s) reveals the reliability of PTM.

Photothermal Image of Nanomaterials. To expand the capability of PTM, we have introduced a scanning mode to PTM, which maps the local heat absorption by scanning a focused heating laser beam across

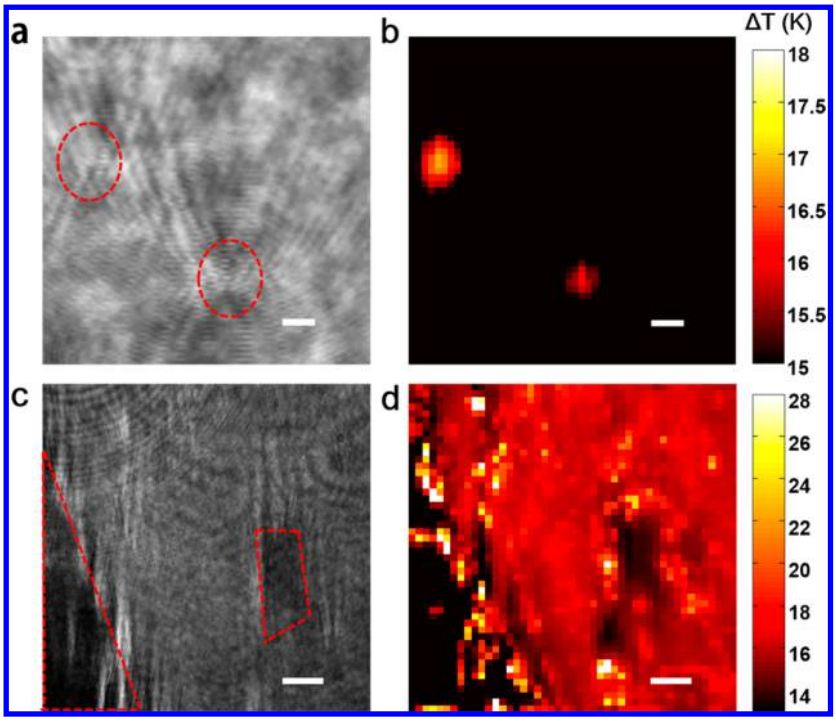

Figure 5. Mapping of heat generation of single GNRs and graphene. (a) Plasmonic image of two gold nanorods marked by dashed circles. (b) Scanning mode PTM image of the gold nanorods in (a). Scale bar: 1 μm. (c) Plasmonic image of graphene with defects (*e.g.*, marked by dashed line). (d) Scanning mode PTM image of the same area with (a). Scale bar: 10 μm.

the sample. The focused laser beam with a diameter of ~1 μm was modulated at a frequency of 10.6 Hz, and the corresponding local temperature variation was obtained by FFT analysis (see the Methods section). To demonstrate the principle of scanning PTM, we applied it to imaging heat generation and dissipation of GNRs. The plasmonic image of two GNRs is shown in Figure 5a, where the red dashed circles mark the positions of the GNRs. The corresponding scanning PTM image is shown in Figure 5b, revealing two spots at the locations of the two GNRs (Figure S6).

PTM can also be used to image the photothermal properties of 2D nanomaterials, such as graphene. Figure 5c shows the plasmonic image of single-layer graphene in water, where the areas outlined by dashed lines are bare gold and the remaining areas are graphene. Because graphene's refractive index is higher than that in the surrounding solution[39] (Figure 5c), the graphene region shows a positive contrast compared with the bare Au region. However, the temperature sensitivities of the bare Au and graphene-covered Au are the same within the experimental error, as shown by calibration experiments (Figure S8).[40] The scanning PTM image of the graphene sample is shown in Figure 5d, which reveals that the graphene areas are brighter than the gold areas. This is because graphene absorbs more laser power, leading to a higher temperature increase compared to the gold areas. The PTM image also reveals many "hot" spots near the edge or defect sites, indicating enhanced photothermal effect at these sites.

Compared to imaging PTM (Figure 3a), the spatial resolution of scanning PTM is determined by the size of the focused laser beam, which is also limited by diffraction. Because the heating laser is focused down to a small spot, scanning PTM can deliver more energy to heat a local area. However, like the previously reported scanning photothermal microscopy,[14] the scanning of a laser beam slows down the imaging speed, which is less suitable for studying fast transient thermal distribution.

CONCLUSIONS

Scanning probe methods, such as SThM, have shown high spatial resolution (down to ~10 nm) and good sensitivity (on the order of mK); however, the slow scanning speed (a few tens of seconds to hundreds of seconds) limits its application mostly on imaging the steady-state temperature distribution. On the other hand, PTM exhibits excellent temporal resolution (10 μs) with good sensitivity (~6 mK), which is particularly suitable for imaging a fast thermal dynamic process, such as thermal generation and diffusion from single nanoparticles in aqueous solutions. Compared to other nonscanning based thermal imaging methods, such as fluorescent probes and infrared cameras, PTM demonstrates much higher sensitivity with comparable spatial resolution. The unique features make PTM a good tool for studying the heat generation and transport associated with local chemical and biochemical reactions in nanomaterials and biological samples.

In conclusion, we have developed plasmonic thermal microscopy and demonstrated a detection limit of ~6 mK, a spatial resolution of a micron (optical diffraction limit), and temporal resolution of 10 μs in water. Using the technique, we have imaged the photothermal effect, heat generation, and dissipation in nanomaterials, including gold nanorods, nanoparticles, and graphene. We have found that the experimental images are in good agreement with simulated images based on finite element analysis. We anticipate that the PTM imaging technology find applications in studying thermal properties in nanomaterials and local heat generation and dissipation in various systems, such as heat arising from external fields, including optical, microwave, and electrical current, and from internal biochemical and electrochemical reactions.

METHODS

Sample Preparation. All of the PTM experiments described here used glass slides coated with 47 nm thick gold film. Each gold-coated slide was annealed with hydrogen flame before the experiment and was then placed on the objective, on which a 0.1 mm thick PDMS cell was attached and filled with DI water. To prevent water evaporation and to focus the heating laser, the cell was covered by a glass slide.

The graphene samples were grown by chemical vapor deposition on top of copper foil and transferred onto a gold substrate with a poly(methyl methacrylate) (PMMA)-mediated approach. A layer of PMMA was coated onto the graphene, and the metal below it was etched away completely. The PMMA/graphene stack was then transferred onto the Au surface.[41] After the graphene was transferred onto the gold substrate, the PMMA layer was dissolved and removed by acetone.

Optical Setup and Data Analysis. The PTM setup was built on an inverted optical microscope.[27,28] A collimated 2 mW 680 nm SLD (www.qphotonics.com) light source was placed behind a linear polarizer to generate p-polarized light for PTM imaging. To generate localized heating, a beam from a 785 nm laser diode (Thorlabs Inc.) was focused on the gold film by a 50× long working distance objective. Two strategies were used to heat nanomaterials in this work: one was to periodically modulate the heating source (laser) at a frequency (10.6 Hz) and to measure the temperature response in every pixel by performing FFT analysis on the plasmonic image intensity. This strategy was used to obtain data in Figures 1, 2, 3, and 5. The second strategy was to turn on the laser power at time 0 with a constant power and monitor the local thermal diffusion kinetics from a single GNR (Figure 4). To remove interference from the heating laser, a 700 nm short-pass filter (Thorlabs Inc.) was placed before the CCD imager. The thermal image was obtained by subtracting the plasmonic image without laser heating from that with laser heating. In order to observe heat generated by single gold nanorods, the heating laser was focused on a target gold nanorod. After recording a thermal image, the laser was moved laterally away from the gold nanorod by 1 μm, and another thermal image was acquired. A differential image was obtained by subtracting the second thermal image from the first one. The thermal images of silica nanoparticles and gold nanoparticles were obtained in a similar way. To observe transient thermal transport at microsecond scale, a fast camera (model) was used to capture thermal images with 10 kfps of frame rate. In the scanning PTM experiments, a piezo-stage was used to scan the sample stage in *x* and *y* directions.

Calibration of PTM. In the calibration experiment, a thermistor (MF52A103J3470, Cantherm) was attached to the gold film in the solution to measure the temperature. Initially, the gold film and thermistor were both immersed in water at room temperature, followed by the addition of hot water. The measured temperature with the thermistor and PTM thermal images from the camera were synchronized using a DAQ card, which allowed the calibration of the thermal images with the temperature reading from the thermistor.

Numerical Simulation. The dependence of the plasmonic signal on the refractive index change of water was calculated with Winspall software v 3.02. In the calculation, four layers, including glass, 2 nm Cr film, 47 nm gold film, and water, were used. The relationship between the resonant angle and refractive index is shown in Figure S2.

Three-dimensional numerical simulations of thermal images were performed with COMSOL multiphysics software v 4.4. The dimensions of the gold film were 16 mm × 12 mm × 47 nm, and a periodic boundary condition was applied to the simulations. The thicknesses of the top water layer and bottom glass slide were 0.16 and 1 mm, respectively. Under the glass slide was a layer of immersion oil with a thickness of 1 mm. For the heat generated by gold film, a 0.25 μm^2 area of the gold film with a uniform heat source of 8.0 mW/μm^2 was used as a boundary condition. To simulate heat generated by a single gold nanorod, the dimensions of the heating source were 40 nm × 40 nm × 140 nm, and the heat flux was set to be 30 mW/μm^2, corresponding to the intensity of the heating laser. The heat transport equation used in the simulation is

$$\rho C_p \frac{\partial T}{\partial t} + \rho C_p \mathbf{u} \nabla T = \nabla(k \nabla T) + Q$$

where ρ, C_p, $\mathbf{u}$, k, and Q are density, heat capacity, flow velocity field, thermal conductivity, and heat source per volume, respectively. The boundary heat source was

$$-\mathbf{n} \cdot (-k \nabla T) = Q_b \quad (4)$$

where Q_b is local heat flux density.

Conflict of Interest: The authors declare no competing financial interest.

Acknowledgment. We thank National Natural Science Foundation of China (NSFC, Grant Nos. 21327008 to N.J.T. and 21427807 to J.J.Z.), Gordon and Betty Moore Foundation, and China Scholarship Council for support.

Supporting Information Available: The Supporting Information is available free of charge on the ACS Publications website at DOI: 10.1021/acsnano.5b05306.

Additional supporting figures (PDF)
PTM imaging of thermal transport generated by heating a gold nanorod for 1 ms (AVI)
Simulated PTM imaging of thermal transport by heating a gold nanorod for 1 ms (AVI)

REFERENCES AND NOTES

1. Yue, Y.; Wang, X. Nanoscale Thermal Probing. *Nano Rev.* **2012**, *3*, 11586.
2. Qin, Z.; Bischof, J. C. Thermophysical and Biological Responses of Gold Nanoparticle Laser Heating. *Chem. Soc. Rev.* **2012**, *41*, 1191–217.
3. Govorov, A. O.; Richardson, H. H. Generating Heat with Metal Nanoparticles. *Nano Today* **2007**, *2*, 30–38.
4. Zijlstra, P.; Paulo, P. M.; Orrit, M. Optical Detection of Single Non-absorbing Molecules Using the Surface Plasmon Resonance of A Gold Nanorod. *Nat. Nanotechnol.* **2012**, *7*, 379–82.
5. Majumdar, A. Scanning Thermal Microscopy. *Annu. Rev. Mater. Sci.* **1999**, *29*, 505–585.
6. Desiatov, B.; Goykhman, I.; Levy, U. Direct Temperature Mapping of Nanoscale Plasmonic Devices. *Nano Lett.* **2014**, *14*, 648–52.
7. Kim, K.; Jeong, W.; Lee, W.; Reddy, P. Ultra-High Vacuum Scanning Thermal Microscopy for Nanometer Resolution Quantitative Thermometry. *ACS Nano* **2012**, *6*, 4248–4257.

8. Yu, Y.-J.; Han, M. Y.; Berciaud, S. p.; Georgescu, A. B.; Heinz, T. F.; Brus, L. E.; Kim, K. S.; Kim, P. High-resolution Spatial Mapping of the Temperature Distribution of a Joule Self-heated Graphene Nanoribbon. *Appl. Phys. Lett.* **2011**, *99*, 183105.
9. Boyer, D.; Tamarat, P.; Maali, A.; Lounis, B.; Orrit, M. Photothermal Imaging of Nanometer-sized Metal Particles Among Scatterers. *Science* **2002**, *297*, 1160–1163.
10. Gaiduk, A.; Yorulmaz, M.; Ruijgrok, P. V.; Orrit, M. Room-temperature Detection of A Single Molecule's Absorption by Photothermal Contrast. *Science* **2010**, *330*, 353–6.
11. Nedosekin, D. A.; Galanzha, E. I.; Dervishi, E.; Biris, A. S.; Zharov, V. P. Super-resolution Nonlinear Photothermal Microscopy. *Small* **2014**, *10*, 135–42.
12. Berciaud, S.; Cognet, L.; Blab, G.; Lounis, B. Photothermal Heterodyne Imaging of Individual Nonfluorescent Nanoclusters and Nanocrystals. *Phys. Rev. Lett.* **2004**, *93*, 257402.
13. Berciaud, S. Observation of Intrinsic Size Effects in the Optical Response of Individual Gold Nanoparticles. *Nano Lett.* **2005**, *5*, 515.
14. Gaiduk, A.; Ruijgrok, P. V.; Yorulmaz, M.; Orrit, M. Detection Limits in Photothermal Microscopy. *Chemical Science* **2010**, *1*, 343.
15. Mecklenburg, M.; Hubbard, W. A.; White, E. R.; Dhall, R.; Cronin, S. B.; Aloni, S.; Regan, B. C. Nanoscale Temperature Mapping in Operating Microelectronic Devices. *Science* **2015**, *347*, 629–632.
16. Yue, Y.; Zhang, J.; Wang, X. Micro/nanoscale Spatial Resolution Temperature Probing for the Interfacial Thermal Characterization of Epitaxial Graphene on 4H-SiC. *Small* **2011**, *7*, 3324–33.
17. Neumann, P.; Jakobi, I.; Dolde, F.; Burk, C.; Reuter, R.; Waldherr, G.; Honert, J.; Wolf, T.; Brunner, A.; Shim, J. H. High-precision Nanoscale Temperature Sensing Using Single Defects in Diamond. *Nano Lett.* **2013**, *13*, 2738–2742.
18. Kucsko, G.; Maurer, P. C.; Yao, N. Y.; Kubo, M.; Noh, H. J.; Lo, P. K.; Park, H.; Lukin, M. D. Nanometre-scale Thermometry in A Living Cell. *Nature* **2013**, *500*, 54–8.
19. Gao, Y.; Bando, Y. Nanotechnology: Carbon Nanothermometer Containing Gallium. *Nature* **2002**, *415*, 599–599.
20. Li, Y.; Li, B. Q. Use of CdTe Quantum Dots for High Temperature Thermal Sensing. *RSC Adv.* **2014**, *4*, 24612.
21. Okabe, K.; Inada, N.; Gota, C.; Harada, Y.; Funatsu, T.; Uchiyama, S. Intracellular Temperature Mapping with a Fluorescent Polymeric Thermometer and Fluorescence Lifetime Imaging Microscopy. *Nat. Commun.* **2012**, *3*, 705.
22. Donner, J. S.; Thompson, S. A.; Kreuzer, M. P.; Baffou, G.; Quidant, R. Mapping Intracellular Temperature Using Green Fluorescent Protein. *Nano Lett.* **2012**, *12*, 2107–11.
23. Wang, X. D.; Wolfbeis, O. S.; Meier, R. J. Luminescent Probes and Sensors for Temperature. *Chem. Soc. Rev.* **2013**, *42*, 7834–69.
24. Baffou, G.; Bon, P.; Savatier, J.; Polleux, J.; Zhu, M.; Merlin, M.; Rigneault, H.; Monneret, S. Thermal Imaging of Nanostructures by Quantitative Optical Phase Analysis. *ACS Nano* **2012**, *6*, 2452–2458.
25. Bae, M. H.; Ong, Z. Y.; Estrada, D.; Pop, E. Imaging, Simulation, and Electrostatic Control of Power Dissipation in Graphene Devices. *Nano Lett.* **2010**, *10*, 4787–93.
26. Ahmad, N.; Stokes, J.; Fox, N. A.; Teng, M.; Cryan, M. J. Ultra-thin Metal Films for Enhanced Solar Absorption. *Nano Energy* **2012**, *1*, 777–782.
27. Shan, X.; Diez-Perez, I.; Wang, L.; Wiktor, P.; Gu, Y.; Zhang, L.; Wang, W.; Lu, J.; Wang, S.; Gong, Q.; Li, J.; Tao, N. Imaging the Electrocatalytic Activity of Single Nanoparticles. *Nat. Nanotechnol.* **2012**, *7*, 668–72.
28. Shan, X.; Patel, U.; Wang, S.; Iglesias, R.; Tao, N. Imaging Local Electrochemical Current *via* Surface Plasmon Resonance. *Science* **2010**, *327*, 1363–1366.
29. Wang, W.; Yang, Y.; Wang, S.; Nagaraj, V. J.; Liu, Q.; Wu, J.; Tao, N. Label-free Measuring and Mapping of Binding Kinetics of Membrane Proteins in Single Living Cells. *Nat. Chem.* **2012**, *4*, 846–853.
30. Wang, W.; Foley, K.; Shan, X.; Wang, S.; Eaton, S.; Nagaraj, V. J.; Wiktor, P.; Patel, U.; Tao, N. Single Cells and Intracellular Processes Studied by A Plasmonic-based Electrochemical Impedance Microscopy. *Nat. Chem.* **2011**, *3*, 249–255.
31. Born, M.; Wolf, E.; Bhatia, A. B. *Principles of Optics: Electromagnetic Theory of Propagation, Interference and Diffraction of Light*; Cambridge University Press, 1999.
32. Shan, X.; Foley, K. J.; Tao, N. A Label-free Optical Detection Method for Biosensors and Microfluidics. *Appl. Phys. Lett.* **2008**, *92*, 133901.
33. Shan, X.; Huang, X.; Foley, K. J.; Zhang, P.; Chen, K.; Wang, S.; Tao, N. Measuring Surface Charge Density and Particle Height Using Surface Plasmon Resonance Technique. *Anal. Chem.* **2010**, *82*, 234–240.
34. Huang, B.; Yu, F.; Zare, R. N. Surface Plasmon Resonance Imaging Using a High Numerical Aperture Microscope Objective. *Anal. Chem.* **2007**, *79*, 2979–2983.
35. Shan, X.; Fang, Y.; Wang, S.; Guan, Y.; Chen, H.-Y.; Tao, N. Detection of Charges and Molecules with Self-assembled Nano-oscillators. *Nano Lett.* **2014**, *14*, 4151–4157.
36. Foley, K. J.; Shan, X.; Tao, N. Surface Impedance Imaging Technique. *Anal. Chem.* **2008**, *80*, 5146–5151.
37. Chen, Z.; Li, J.; Chen, X.; Cao, J.; Zhang, J.; Min, Q.; Zhu, J. J. Single Gold@Silver Nanoprobes for Real-time Tracing the Entire Autophagy Process at Single-cell Level. *J. Am. Chem. Soc.* **2015**, *137*, 1903–8.
38. Baffou, G.; Rigneault, H. Femtosecond-pulsed Optical Heating of Gold Nanoparticles. *Phys. Rev. B: Condens. Matter Mater. Phys.* **2011**, *84*, 035415.
39. Ni, Z. H.; Wang, H. M.; Kasim, J.; Fan, H. M.; Yu, T.; Wu, Y. H.; Feng, Y. P.; Shen, Z. X. Graphene Thickness Determination Using Reflection and Contrast Spectroscopy. *Nano Lett.* **2007**, *7*, 2758–2763.
40. Shan, X.; Chen, S.; Wang, H.; Chen, Z.; Guan, Y.; Wang, Y.; Wang, S.; Chen, H.-Y.; Tao, N. Mapping Local Quantum Capacitance and Charged Impurities in Graphene via Plasmonic Impedance Imaging. *Adv. Mater.* **2015**, 10.1002/adma.201502822.
41. Li, X.; Zhu, Y.; Cai, W.; Borysiak, M.; Han, B.; Chen, D.; Piner, R. D.; Colombo, L.; Ruoff, R. S. Transfer of Large-Area Graphene Films for High-Performance Transparent Conductive Electrodes. *Nano Lett.* **2009**, *9*, 4359–4363.